Letter

Second-harmonic generation in the topological multifold semimetal RhSi

Baozhu Lu,[1] Sharareh Sayyad,[2,3] Miguel Ángel Sánchez-Martínez,[2] Kaustuv Manna,[4,5] Claudia Felser,[4] Adolfo G. Grushin,[2,*] and Darius H. Torchinsky[1,†]

[1]*Department of Physics, Temple University, Philadelphia, Pennsylvania 19122, USA*
[2]*Univ. Grenoble Alpes, CNRS, Grenoble INP, Institut Néel, 38000 Grenoble, France*
[3]*Max Planck Institute for the Science of Light, Staudtstraße 2, 91058 Erlangen, Germany*
[4]*Max Planck Institute for Chemical Physics of Solids, Dresden D-01187, Germany*
[5]*Department of Physics, Indian Institute of Technology Delhi, New Delhi 110016, India*

(Received 18 February 2021; revised 14 May 2021; accepted 8 April 2022; published 26 April 2022)

Recent experiments in the topological Weyl semimetal TaAs have observed record-breaking second-harmonic generation (SHG), a nonlinear optical response at 2ω generated by an incoming light source at ω. However, whether SHG is enhanced in topological semimetals in general is a challenging open question because their band structure entangles the contributions arising from trivial bands and topological band crossings. In this work, we circumvent this problem by studying RhSi, a chiral topological semimetal with a simple band structure with topological multifold fermions close to the Fermi energy. We measure SHG in a wide frequency window, $\omega \in [0.27, 1.5]$ eV and, using first-principles calculations, we establish that, due to their linear dispersion, the contribution of multifold fermions to SHG is subdominant as compared with other regions in the Brillouin zone. Our calculations suggest that parts of the bands where the dispersion is relatively flat contribute significantly to SHG. As a whole, our results suggest avenues to enhance SHG responses.

DOI: 10.1103/PhysRevResearch.4.L022022

I. INTRODUCTION

Second-harmonic generation (SHG) is a nonlinear optical response that is useful in interrogating quantum phases of matter; since it only occurs in media without inversion symmetry, it is used as a proxy for spontaneous symmetry breaking [1–6] and in studies of the surface and interfacial properties of materials [7–12]. It is also widely applied technologically as the basis for generating light sources at different wavelengths [13,14]. Therefore finding systems without inversion symmetry and with a high second-harmonic yield is a contemporary material science challenge.

A central challenge to finding materials with a large SHG is identifying the microscopic origin of large nonlinear optical responses. In two recent experiments [15,16], the topological semimetal TaAs [17–23] was reported to exhibit a giant SHG response at $\omega \sim 1.5$ eV (800 nm) [15], reaching a maximum yield $\sim 2 \times 10^2$ larger than the maximum response of the semiconductor GaAs at 0.7 eV incoming photon energy [16]. The $\sim$eV frequencies at which the band structure was probed, however, were far larger than the $\sim$60 meV energy scale associated with the topological degeneracies of its low-energy band structure, the Weyl nodes. Hence the existence of Weyl nodes cannot explain the enhanced response. Instead, the enhancement was attributed phenomenologically to the skewness of the polarization distribution [16], but a general microscopic origin has yet to be uncovered. Moreover, the role of topological degeneracies with linear dispersion, such as Weyl nodes, in determining SHG remains experimentally unclear mainly due to the complex band structure of TaAs when probed at large ($\sim$eV) frequencies [15,16,24].

In this work, we show experimentally, and demonstrate theoretically that transitions between linearly dispersing bands, specifically those close to topological band degeneracies, suppress rather than enhance SHG. We do so by studying the chiral topological semimetal RhSi in space group 198, which has a relatively simple band structure [25–28] as compared with TaAs [18,29]. Close to the Fermi energy (E_F) three and four bands meet at the Brillouin center and corner, respectively, resulting in two topological degenerate points known as multifold nodes [30–33,33]. Additionally, the cubic symmetry and the absence of inversion and mirror symmetries in space group 198 simplify the analysis of SHG from RhSi because, unlike TaAs, there is only one independent component of the SHG tensor, χ^{xyz}. The simplicity of this space group has aided the interpretation of other nonlinear optical responses, notably the circular-photogalvanic effect [34–36]

We report χ^{xyz} of RhSi over a wide frequency range (see Fig. 1), i.e., from 0.27 to 1.55 eV, and compare it with first-principles calculations which, at low energies, are also benchmarked with a $k \cdot p$ model [36]. By identifying the regions in the band structure connected by optical transitions, we can infer that contributions between linearly dispersing bands are relatively small compared with those regions with relatively flat dispersion. When linear contributions are active

*adolfo.grushin@neel.cnrs.fr.
†dtorchin@temple.edu.

Published by the American Physical Society under the terms of the Creative Commons Attribution 4.0 International license. Further distribution of this work must maintain attribution to the author(s) and the published article's title, journal citation, and DOI. Open access publication funded by the Max Planck Society.

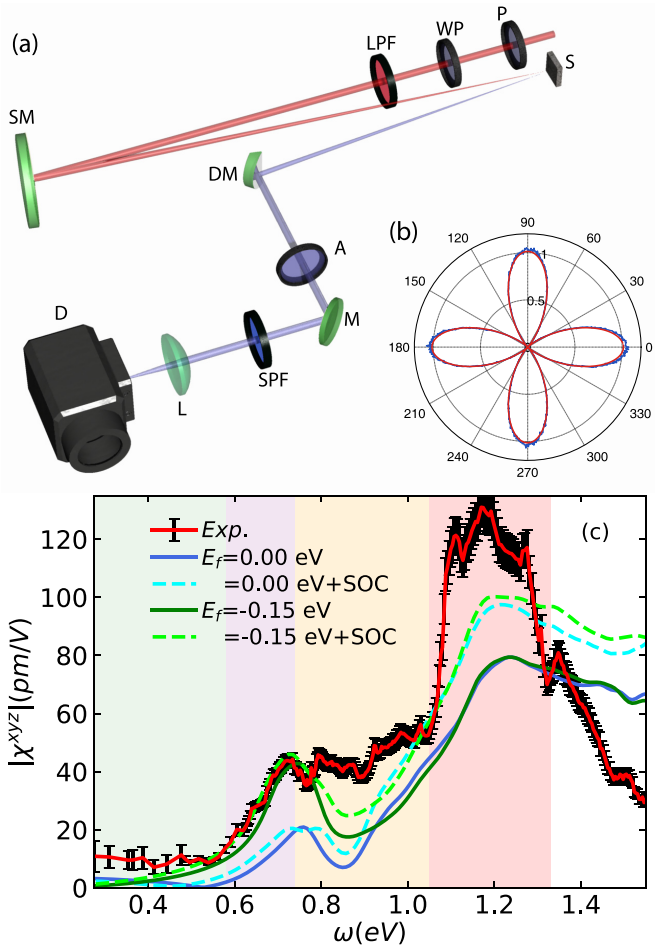

FIG. 1. (a) Schematic diagram of setup used in SHG measurements. Optics are P, polarizer; WP, waveplate; LPF, longpass filter; SM, spherical mirror; S, sample; DM, D-shaped mirror; A, analyzer; M, mirror; SPF, shortpass filter; L, lens; D, detector. (b) Representative data and fit for $\omega = 1.24$ eV. The data are in blue while the fit to Eq. (A2) in Ref. [53] is in red. (c) Experimentally measured (red line with black error bars) and theoretically calculated (colored lines) SHG susceptibilities. Fermi energies are indicated by colors $E_f = 0.0$ (blue), -0.15 (green) eV. Solid (dashed) lines present theoretical results without (with) SOC. The scissors potential is $\Delta = 1.23$ eV. Shaded areas represent the photon energies at which different transitions from the valance to conduction bands occur. See also Figs. 2(a) and 3(a) for examples of these transitions. Shaded areas span $\omega \in [0.276, 0.58]$ (green), [0.58,0.74] (purple), [0.74,1.05] (orange), and [1.05,1.33] (red) eV. For the definition of the error bars, see the Supplemental Material [53].

(green and yellow regions in Fig. 1), the increase of the SHG signal as a function of frequency is relatively small compared with other frequency regions (purple and red regions in Fig. 1). We refer to this smaller contribution as a suppression of the SHG signal. The best agreement with the data is obtained after correcting the bare separation between bands by incorporating many-body effects [37–41], suggesting that capturing other nonlinear responses in chiral topological semimetals may require these corrections as well.

At the single-particle level, the suppression of SHG from transitions involving to linear bands compared with transitions involving other types of bands can be understood from dimensional analysis [42,43]; since the SHG susceptibility χ has units of inverse energy squared (in units of fundamental constants) and the linear bands have no associated energy scale, the first finite contribution to SHG is due to quadratic corrections to the linear bands. This contribution is frequency independent because, by dimensional analysis, the SHG may scale as $1/t^2$ where t is inversely related to the band curvature. Hence linear bands, where t is large, have smaller contributions than other points in the Brillouin zone. In contrast, flatter parts of the Brillouin zone contribute with a larger density of states, resulting in a comparatively larger SHG.

RhSi crystalizes in the cubic space group $P2_13$ (number 198). Several materials in this space group, notably CoSi, RhSi, AlPt, PdGa, and PtGa [25–27,44–49], are known chiral topological semimetals that lack inversion and mirror symmetries [30–33]. Photoemission experiments revealed that these materials showed spectra consistent with a threefold degeneracy at the Γ point and a fourfold degeneracy at the zone corner [27,44–47]. These are topological band degeneracies and lead to exotic photogalvanic effects, including a quantized circular photogalvanic effect [25,50–52], which has been proven to be challenging to observe [34–36].

II. EXPERIMENT

Figure 1(a) shows a schematic diagram of our SHG setup. The output of a regeneratively amplified Ti:sapph laser producing 1.2 mJ, 35-fs pulses centered at 800 nm at a repetition rate of 5 kHz was used to pump an optical parametric amplifier (OPA) from which we derived the incoming fundamental laser field in the 800 nm–4.5 μm wavelength range ($0.276 - 1.55$ eV). More details on the experimental system can be found in the Supplemental Material [53]. The intensity of the vertically polarized SHG output was measured as a function of incoming polarization angle ϕ, an example of which is shown in Fig. 1(b) with a typical fit to the expression $2/3[\chi^{xyz}\cos(2\phi)]^2$. The fits were corrected for the experimental parameters of pulse duration, spot size, and instrument response and then normalized against a GaAs standard in order to arrive at an absolute quantitative value for the SHG susceptibility element χ^{xyz}, with results in a ratio $\chi^{xyz}_{\mathrm{GaAs}}/\chi^{xyz}_{\mathrm{RhSi}} = 2.4$ for photon energy $\omega = 1.24$ eV. This calibration procedure is described in detail in Ref. [16]. The resulting SHG in the $0.27 - 1.5$ eV energy range is shown in Fig 1(c). We note that this spectrum covers over five octaves of bandwidth and reaches, to our knowledge, a far lower energy than any SHG previously reported.

III. THEORY

We have carried out the density functional theory (DFT) calculation using the EXCITING package [54] based on state-of-the-art full-potential linearized augmented plane-wave implementations. We have employed the generalized gradient approximations within the Perdew-Burke-Ernzerhof scheme [55] as an exchange-correlation functional. The lattice parameters of the chiral cubic crystal RhSi have been chosen based on experimental measurements [25,56]. Four atoms of Rh and four atoms of Si in the unit cell are located in the Wyckoff positions for the space group $P2_13$ [27,56]. We have

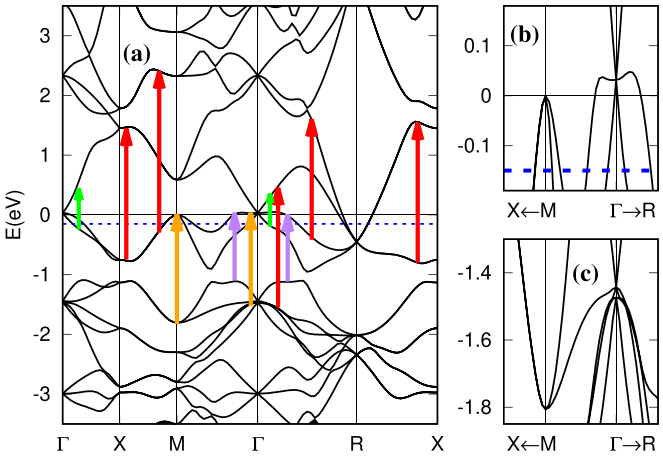

FIG. 2. (a) First-principles band structure of RhSi without SOC. Arrows indicate representative two-photon electronic transitions in SHG, and their color code corresponds to that of the shaded areas representing different frequency windows in Fig. 1(c). (b) Zoom to the low-energy bands between Γ and M points close to the Fermi level. Dashed lines indicate the Fermi energy at which the theoretical curves in Fig. 1(c) are plotted, namely, $E_f = -0.15$ (blue) eV. (c) Same as (b) but close to energy -1.6 eV. The zero of energy scale represents the Fermi energy of the pristine system.

performed our calculations on a $50 \times 50 \times 50$ k-point grid. In the following, we present our results in the presence and absence of the spin-orbit coupling (SOC).

The electronic band structure for RhSi along the lines connecting high-symmetry points in the Brillouin zone is shown in Fig. 2 when SOC is not included and in Fig. 3 in the presence of SOC. The energy is measured with respect to the Fermi energy of the pristine system $E_f = 0$ eV. Close to

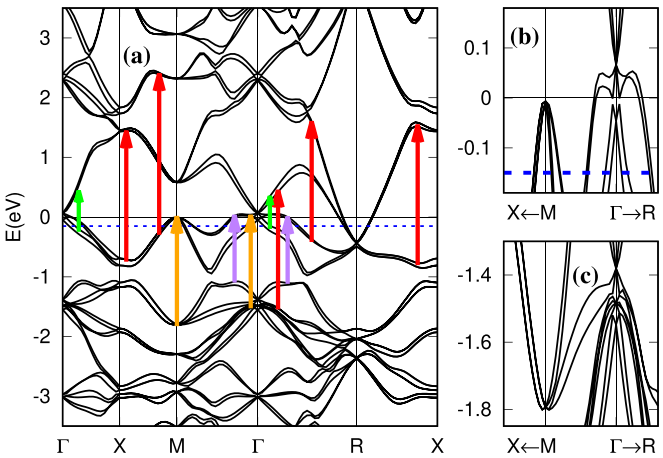

FIG. 3. (a) First-principles band structure of RhSi with SOC. Arrows indicate representative two-photon electronic transitions in SHG, and their color code corresponds to that of the shaded areas representing different frequency windows in Fig. 1(c). (b) Zoom to the low-energy bands between the Γ and M points close to the Fermi level. Dashed lines indicate the Fermi energy at which the theoretical curves in Fig. 1(c) are plotted, namely, $E_f = -0.15$ eV. (c) Same as (b) but close to energy -1.6 eV. The zero of energy scale represents the Fermi energy of the pristine system.

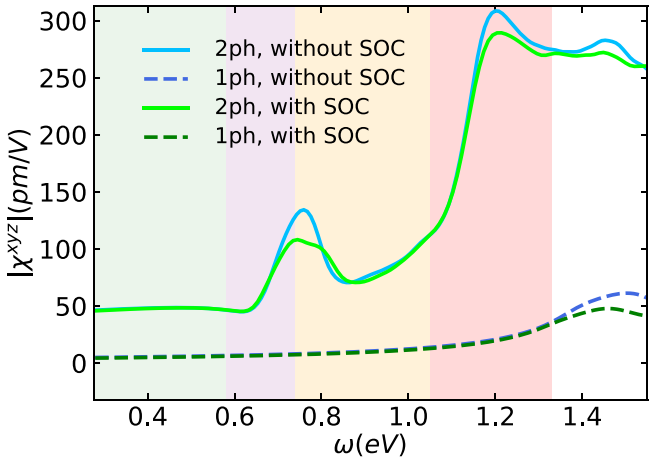

FIG. 4. Calculated different components of SHG from two-photon (solid sky blue line), one-photon (dashed royal blue line) transitions calculated without SOC as well as two-photon (solid green line), one-photon (dashed dark green line) transitions in the presence of SOC. Both sets of results are at Fermi energy $E_f = -0.15$ eV. The total SHG susceptibility is plotted in Fig. 1(c) and scissors potential $\Delta = 1.23$ eV.

the Fermi energy, the electronic structure possesses a threefold degeneracy at the Γ point, Fig. 2(b) and Fig. 3(b), and a fourfold degenerate point at the R point. We note that degenerate threefold crossings also exist at different energies at the Γ point, e.g., around $E \approx -1.57$ eV, a region magnified in Fig. 2(c) and Fig. 3(c).

Our *ab initio* results for the nonlinear susceptibility χ^{xyz} of RhSi are shown in Fig. 1(c); see Ref. [53] for more details. As in the experimental analysis, we also calibrate our results with GaAs [57]. The position of the Fermi energy in our system is determined indirectly, as in other optics experiments [35,36]. To account for the effects of disorder and finite temperature in our experimental sample, we have employed a Gaussian broadening with width $\delta = 0.1$ eV, consistent with previous findings [35]. We also include a scissors shift [39] of $\Delta = 1.23$ eV to account for renormalized occupied and unoccupied bands due to many-body effects; see Ref. [53].

Our results for RhSi, for Fermi energies that lie below the threefold node ($0.0 - 0.15$ eV) in the presence/absence of SOC, are shown in Fig. 1(c). For RhSi, we observe that for $\omega \lesssim 0.6$ eV, theory (with/without SOC) and experiment are in reasonable agreement. One should note that for $\omega < 0.4$, the agreement between theory and four data points of the experiment deteriorates in which the experimental data exhibit nearly 50% errors. This low-energy regime is, not coincidentally, where the experiment is extraordinarily challenging to perform due to both a lack of sensitive detection technology and an absence of standard candle calibrants.

The small SHG yield in the green frequency window $\omega \in [0.276, 0.58]$ in Fig. 1(c) is a result of the suppressed optical transitions between low-energy linearly dispersing bands close to the Γ point; see green arrows in Figs. 2 and 3. To support this conclusion we first separate one-photon (ω) and two-photon (2ω) transitions contributing to χ^{xyz} in Fig. 4. We observe that two-photon transitions dominate the green frequency region regardless including or excluding the SOC.

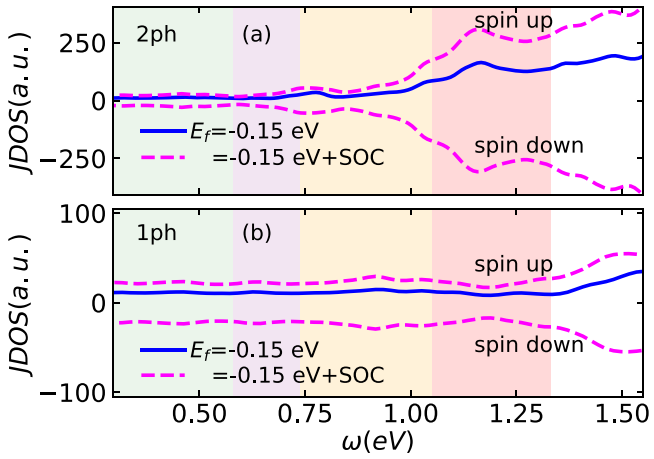

FIG. 5. Optical joint density of states for SHG from two-photon (a) and one-photon (b) contributions calculated without SOC (solid blue lines) and in the presence of SOC (dashed magenta lines). In the presence of SOC, spin-resolved JDOS is plotted. Note the different vertical scales in each panel.

Next, we compare this result to the two-photon and one-photon joint density of states (JDOS) in Figs. 5(a) and 5(b), respectively. The JDOS counts allowed optical transitions between occupied (with energy ω_n) and unoccupied (with energy ω_m) states ignoring their associated matrix elements, i.e., $\mathrm{JDOS}(\Omega) = \sum_{m,n} \delta(\omega_m - \omega_n - \Omega)$, where $\Omega = 2\omega\,(= \omega)$ for the two-(one-)photon JDOS. In the green frequency window, the one-photon JDOS dominates compared with the two-photon JDOS, cf. Figs. 5(a) and 5(b). Comparing with Fig. 4, this indicates that the optical matrix elements suppress the one-photon contribution to χ^{xyz}, reducing the overall SHG for $\omega < 0.58\,\mathrm{eV}$. The band structures in Figs. 2 and 3 suggest that the contribution to one-photon processes in this frequency region arises from linear bands around Γ, whose matrix elements therefore suppress SHG.

In order to further understand the low-energy region and to benchmark our DFT calculations, we have developed a low-energy $k \cdot p$ model; see the Supplemental Material [53]. This model captures low-energy excitations around the Γ point and brings insight into understanding the optical transitions resulting from the threefold node. Specifically, the SHG response around Γ displays a broad, low-energy peak below the experimentally accessible frequencies. This single peak results from the merging of a dominant two-photon peak with a subdominant one-photon peak due to the large $\delta \approx 100$ meV. A qualitatively similar broadened peak is also present by DFT when $\Delta = 0$, which additionally receives contributions not captured by the $k \cdot p$ model. Consequently, the DFT peak is broader compared with that found using the $k \cdot p$ model. When $\Delta \neq 0$, the DFT results show that this low-energy peak is largely suppressed. This is because Δ is a correction that pushes occupied and empty bands away from each other, and thus the optical transitions responsible for the peak are pushed to higher energies, resulting in a better agreement with the experimental data. These results highlight the fact that both the many-body corrections, modeled with a scissors potential Δ, and the quasiparticle broadening δ are essential to explain the experimental measurements.

In addition, we note that the scissors potential Δ favors two-photon contributions. The reason is that, by separating occupied and unoccupied states, Δ reduces the available phase space for one-photon transitions with $\omega < \Delta$. In contrast, the phase space for two-photon transitions is only reduced for lower photon energies, $\omega < \Delta/2$. As a result, two-photon transitions dominate for $\omega < \Delta$, as seen in Fig. 4.

We move on to analyze the purple frequency window in Fig. 1(c), i.e., $\omega \in [0.58, 0.74]\,\mathrm{eV}$. The SHG increases in this region, a feature that is well captured in our calculation when $E_f < 0\,\mathrm{eV}$ irrespective of whether SOC is included or not. Separately plotting one- and two-photon contributions as before in Fig. 4 reveals that the two-photon response in the purple energy window is dominant. Consistent with our discussion in the previous paragraph, the rise of the two-photon contributions occurs around $\omega \approx \Delta/2$ in the JDOS. When compared with the band structure, the observation of a dominant two-photon transition in Fig. 4 suggests that two partially flat bands close to the Γ point, separated by approximately 1.3 eV and connected by two-photon excitations (purple arrows) in Figs. 2 and 3, are responsible for enhancing χ^{xyz} in the purple energy window. The width of this energy window is comparable to the quasiparticle broadening ($\delta = 0.1\,\mathrm{eV}$), supporting their flat band origin.

At photon energies $\omega \in [0.74, 1.05]\,\mathrm{eV}$, i.e., in the orange window in Fig. 1(c), the data exhibit a plateaulike structure. Our DFT calculations show that this feature is reproduced better when SOC is present for $E_f = -0.15\,\mathrm{eV}$. Naively, one would expect that in this frequency window, the one-photon electronic transitions from linear bands close to the R point are activated. However, Figs. 4 and 5 reveal that the one-photon contribution (dashed lines) is small compared with the dominant two-photon transitions. The small contribution of the linearly dispersing bands close to the R point is expected by dimensional analysis and confirmed by our results. The two-photon transitions responsible for SHG in this region likely involve dispersing valance bands around the M and Γ points, as indicated by the orange arrows in Figs. 2 and 3.

Last, there is a drastic increase of χ^{xyz} measured within the red energy window of $\omega \in [1.05, 1.33]\,\mathrm{eV}$ in Fig. 1(c). Our theoretical results also report an increased SHG yield in this energy range with a sharper rise when SOC is included. Once more we can identify the substantial role of two-photon transitions compared with the smaller one-photon contribution; see Figs. 4 and 5. The large photon energies that define this energy window enable electrons to reach a considerable number of bands exemplified by red arrows in Figs. 2 and 3. As frequency increases, we observe quantitative differences between our DFT results and the experimental measurements, especially when $\omega > 1.33\,\mathrm{eV}$. These deviations could be attributed to the insufficient many-body corrections in our first-principles calculations.

IV. CONCLUSIONS

In summary, our SHG spectra on RhSi together with our first principles and $k \cdot p$ calculations show that one-photon transitions among relatively linear bands have a small contribution to SHG. Because of the linear dispersion, these transitions are suppressed compared with the dominant

two-photon transitions among other types of dispersive bands including those between relatively flat bands, account for the observed SHG signal. At the single-particle level, this result is consistent with the expectation that one-photon transitions are more likely to connect linear bands close to E_f, which are expected by dimensional analysis to suppress the SHG. An additional, many-body effect results from a sizable scissors potential Δ, which separates occupied and unoccupied states and favors two-photon over one-photon transitions. We expect that materials in the same space group such as AlPt [46], PdGa [47,49], and PtGa [48] behave similarly.

Our findings complement earlier observations that predict the enhancement of SHG due to other factors, such as the skewness of the polarization distribution [16] or a significant intersite hopping [58]. Taken together, these results outline strategies to find materials with high SHG yield.

ACKNOWLEDGMENTS

S.S. thanks G. Davino for his suggestions on improving DFT calculations. We thank F. de Juan, J. E. Moore, T. Morimoto, J. Orenstein, D. Parker, L. Wu, and Y. Zhang for discussions and related collaborations. A.G.G. and S.S. acknowledge funding by the ANR under Grant ANR-18-CE30-0001-01 (TOPODRIVE). A.G.G. is also funded by the European Union Horizon 2020 research and innovation program under Grant Agreement No. 829044 (SCHINES). M.A.S.M. is supported by the European Union's Horizon 2020 research and innovation programme under the Marie-Sklodowska-Curie Grant Agreement No. 754303 and the GreQuE Cofund programme. D.H.T. acknowledges Temple University startup funding. K.M. and C.F. acknowledge the financial support from the European Research Council (ERC) Advanced Grant No. 742068 "TOP-MAT," European Union's Horizon 2020 research and innovation program (Grants No. 824123 and No. 766566), and Deutsche Forschungsgemeinschaft (DFG) through SFB 1143. K.M. acknowledges the Max Planck Society for the funding support under Max Planck-India partner group project. The work at Temple University was funded in part by the National Science Foundation under Award No. NSF/DMR-1945222.

B.L. and S.S. contributed equally.

[1] Y. R. Shen, Surface second harmonic generation: A new technique for surface studies, Annu. Rev. Mater. Sci. **16**, 69 (1986).

[2] Y. R. Shen, Surface properties probed by second-harmonic and sum-frequency generation, Nature (London) **337**, 519 (1989).

[3] A. Dähn, W. Hübner, and K. H. Bennemann, Symmetry Analysis of the Nonlinear Optical Response: Second Harmonic Generation at Surfaces of Antiferromagnets, Phys. Rev. Lett. **77**, 3929 (1996).

[4] J. C. Petersen, M. D. Caswell, J. S. Dodge, I. A. Sergienko, J. He, R. Jin, and D. Mandrus, Nonlinear optical signatures of the tensor order in $Cd_2Re_2O_7$, Nat. Phys. **2**, 605 (2006).

[5] J. W. Harter, Z. Y. Zhao, J.-Q. Yan, D. G. Mandrus, and D. Hsieh, A parity-breaking electronic nematic phase transition in the spin-orbit coupled metal Cd_2 Re_2 O_7, Science **356**, 295 (2017).

[6] N. Sirica, P. P. Orth, M. S. Scheurer, Y. M. Dai, M. C. Lee, P. Padmanabhan, L. T. Mix, S. W. Teitelbaum, M. Trigo, L. X. Zhao, G. F. Chen, B. Xu, R. Yang, B. Shen, C. C. Lee, H. Lin, T. A. Cochran, S. A. Trugman, J. X. Zhu, M. Z. Hasan *et al.*, Photocurrent-driven transient symmetry breaking in the Weyl semimetal TaAs, Nat. Mater. **21**, 62 (2022).

[7] V. Mizrahi and J. E. Sipe, Phenomenological treatment of surface second-harmonic generation, J. Opt. Soc. Am. B **5**, 660 (1988).

[8] R.-P. Pan, H. D. Wei, and Y. R. Shen, Optical second-harmonic generation from magnetized surfaces, Phys. Rev. B **39**, 1229 (1989).

[9] Y. M. Chang, L. Xu, and H. W. K. Tom, Observation of Coherent Surface Optical Phonon Oscillations by Time-Resolved Surface Second-Harmonic Generation, Phys. Rev. Lett. **78**, 4649 (1997).

[10] A. Kirilyuk and T. Rasing, Magnetization-induced-second-harmonic generation from surfaces and interfaces, J. Opt. Soc. Am. B **22**, 148 (2005).

[11] D. Hsieh, J. W. McIver, D. H. Torchinsky, D. R. Gardner, Y. S. Lee, and N. Gedik, Nonlinear Optical Probe of Tunable Surface Electrons on a Topological Insulator, Phys. Rev. Lett. **106**, 057401 (2011).

[12] C. Lee, F. Katmis, P. Jarillo-Herrero, J. S. Moodera, and N. Gedik, Direct measurement of proximity-induced magnetism at the interface between a topological insulator and a ferromagnet, Nat. Commun. **7**, 1 (2016).

[13] 2. far-infrared wave generation, in *Physical Principles of Far-Infrared Radiation*, Methods in Experimental Physics, edited by L.C. Robinson (Academic Press, 1973), Vol. 10, pp. 10–81.

[14] J. Zhao, J. Fan, W. Liu, H. Shi, N. Xiao, and M. Hu, Ultra-broadband second-harmonic generation in ZnO nano-tetrapod with over-one-octave bandwidth, IEEE Photonics Technol. Lett. **31**, 250 (2019).

[15] L. Wu, S. Patankar, T. Morimoto, N. L. Nair, E. Thewalt, A. Little, J. G. Analytis, J. E. Moore, and J. Orenstein, Giant anisotropic nonlinear optical response in transition metal monopnictide Weyl semimetals, Nat. Phys. **13**, 350 (2017).

[16] S. Patankar, L. Wu, B. Lu, M. Rai, J. D. Tran, T. Morimoto, D. E. Parker, A. G. Grushin, N. L. Nair, J. G. Analytis, J. E. Moore, J. Orenstein, and D. H. Torchinsky, Resonance-enhanced optical nonlinearity in the Weyl semimetal TaAs, Phys. Rev. B **98**, 165113 (2018).

[17] N. P. Armitage, E. J. Mele, and A. Vishwanath, Weyl and Dirac semimetals in three-dimensional solids, Rev. Mod. Phys. **90**, 015001 (2018).

[18] H. Weng, C. Fang, Z. Fang, B. A. Bernevig, and X. Dai, Weyl Semimetal Phase in Noncentrosymmetric Transition-Metal Monophosphides, Phys. Rev. X **5**, 011029 (2015).

[19] B. Q. Lv, H. M. Weng, B. B. Fu, X. P. Wang, H. Miao, J. Ma, P. Richard, X. C. Huang, L. X. Zhao, G. F. Chen, Z. Fang, X. Dai, T. Qian, and H. Ding, Experimental Discovery of Weyl Semimetal TaAs, Phys. Rev. X **5**, 031013 (2015).

[20] S.-Ming Huang, S.-Y. Xu, I. Belopolski, C.-C. Lee, G. Chang, B. Wang, N. Alidoust, G. Bian, M. Neupane, C. Zhang, S. Jia, A. Bansil, H. Lin, and M. Hasan, A Weyl fermion semimetal with surface Fermi arcs in the transition metal monopnictide TaAs class, Nat. Commun. **6**, 7373 (2015).

[21] L. X. Yang, Z. K. Liu, Y. Sun, H. Peng, H. F. Yang, T. Zhang, B. Zhou, Y. Zhang, Y. F. Guo, M. Rahn, D. Prabhakaran, Z. Hussain, S. K. Mo, C. Felser, B. Yan, and Y. L. Chen, Weyl semimetal phase in the non-centrosymmetric compound TaAs, Nat. Phys. **11**, 728 (2015).

[22] S.-Y. Xu, I. Belopolski, N. Alidoust, M. Neupane, G. Bian, C. Zhang, R. Sankar, G. Chang, Z. Yuan, C.-C. Lee *et al.*, Discovery of a Weyl fermion semimetal and topological Fermi arcs, Science **349**, 613 (2015).

[23] B. Q. Lv, N. Xu, H. M. Weng, J. Z. Ma, P. Richard, X. C. Huang, L. X. Zhao, G. F. Chen, C. E. Matt, F. Bisti *et al.*, Observation of weyl nodes in taas, Nat. Phys. **11**, 724 (2015).

[24] Z. Li, Y.-Q. Jin, T. Tohyama, T. Iitaka, J.-X. Zhang, and H. Su, Second harmonic generation in the Weyl semimetal TaAs from a quantum kinetic equation, Phys. Rev. B **97**, 085201 (2018).

[25] G. Chang, S.-Y. Xu, B. J. Wieder, D. S. Sanchez, S.-M. Huang, I. Belopolski, T.-R. Chang, S. Zhang, A. Bansil, H. Lin, and M. Z. Hasan, Unconventional Chiral Fermions and Large Topological Fermi Arcs in RhSi, Phys. Rev. Lett. **119**, 206401 (2017).

[26] P. Tang, Q. Zhou, and S.-C. Zhang, Multiple Types of Topological Fermions in Transition Metal Silicides, Phys. Rev. Lett. **119**, 206402 (2017).

[27] D. S. Sanchez, I. Belopolski, T. A. Cochran, X. Xu, J. X. Yin, G. Chang, W. Xie, K. Manna, V. Süß, C. Y. Huang, N. Alidoust, D. Multer, S. S. Zhang, N. Shumiya, X. Wang, G. Q. Wang, T. R. Chang, C. Felser, S. Y. Xu, S. Jia *et al.*, Topological chiral crystals with helicoid-arc quantum states, Nature (London) **567**, 500 (2019).

[28] T. A. Cochran, G. Chang, I. Belopolski, K. Manna, D. S. Sanchez, Z. Chéng, J.-X. Yin, H. Borrmann, J. Denlinger, C. Felser, H. Lin, and M. Zahid Hasan, A Fermi Arc Quantum Ladder, arXiv:2004.11365 (2020).

[29] J. Buckeridge, D. Jevdokimovs, C. R. A. Catlow, and A. A. Sokol, Bulk electronic, elastic, structural, and dielectric properties of the Weyl semimetal TaAs, Phys. Rev. B **93**, 125205 (2016).

[30] J. L. Mañes, Existence of bulk chiral fermions and crystal symmetry, Phys. Rev. B **85**, 155118 (2012).

[31] B. J. Wieder, Y. Kim, A. M. Rappe, and C. L. Kane, Double Dirac Semimetals in Three Dimensions, Phys. Rev. Lett. **116**, 186402 (2016).

[32] B. Bradlyn, J. Cano, Z. Wang, M. G. Vergniory, C. Felser, R. J. Cava, and B. A. Bernevig, Beyond Dirac and Weyl fermions: Unconventional quasiparticles in conventional crystals, Science **353**, aaf5037 (2016).

[33] G. Chang, B. J. Wieder, F. Schindler, D. S. Sanchez, I. Belopolski, S.-M. Huang, B. Singh, D. Wu, T.-R. Chang, T. Neupert *et al.*, Topological quantum properties of chiral crystals, Nat. Mater. **17**, 978 (2018).

[34] D. Rees, K. Manna, B. Lu, T. Morimoto, H. Borrmann, C. Felser, J. E. Moore, D. H. Torchinsky, and J. Orenstein, Helicity-dependent photocurrents in the chiral Weyl semimetal RhSi, Sci. Adv. **6**, eaba0509 (2020).

[35] Z. Ni, B. Xu, M.-Á. Sánchez-Martínez, Y. Zhang, K. Manna, C. Bernhard, J. W. F. Venderbos, F. de Juan, C. Felser, A. G. Grushin, and L. Wu, Linear and nonlinear optical responses in the chiral multifold semimetal RhSi, npj Quantum Mater. **5**, 96(2020).

[36] Z. Ni, K. Wang, Y. Zhang, O. Pozo, B. Xu, X. Han, K. Manna, J. Paglione, C. Felser, A. G. Grushin *et al.*, Giant topological longitudinal circular photo-galvanic effect in the chiral multifold semimetal CoSi, Nat. Commun. **12** (2021).

[37] Z. H. Levine and D. C. Allan, Linear Optical Response in Silicon and Germanium Including Self-Energy Effects, Phys. Rev. Lett. **63**, 1719 (1989).

[38] J. L. P. Hughes and J. E. Sipe, Calculation of second-order optical response in semiconductors, Phys. Rev. B **53**, 10751 (1996).

[39] F. Nastos, B. Olejnik, K. Schwarz, and J. E. Sipe, Scissors implementation within length-gauge formulations of the frequency-dependent nonlinear optical response of semiconductors, Phys. Rev. B **72**, 045223 (2005).

[40] B. Sadhukhan, Y. Zhang, R. Ray, and J. van den Brink, First-principles calculation of shift current in chalcopyrite semiconductor $ZnSnP_2$, Phys. Rev. Mater. **4**, 064602 (2020).

[41] W. Song, G.-Y. Guo, S. Huang, L. Yang, and L. Yang, First-principles studies of second-order nonlinear optical properties of organic-inorganic hybrid halide perovskites, Phys. Rev. Appl. **13**, 014052 (2020).

[42] X. Yang, K. Burch, and Y. Ran, Divergent bulk photovoltaic effect in Weyl semimetals, arXiv:1712.09363.

[43] O. Pozo and F. de Juan, Computing observables without eigenstates: Applications to bloch hamiltonians, Phys. Rev. B **102**, 115138 (2020).

[44] Z. Rao, H. Li, T. Zhang, S. Tian, C. Li, B. Fu, C. Tang, L. Wang, Z. Li, W. Fan *et al.*, Observation of unconventional chiral fermions with long Fermi arcs in CoSi, Nature (London) **567**, 496 (2019).

[45] D. Takane, Z. Wang, S. Souma, K. Nakayama, T. Nakamura, H. Oinuma, Y. Nakata, H. Iwasawa, C. Cacho, T. Kim, K. Horiba, H. Kumigashira, T. Takahashi, Y. Ando, and T. Sato, Observation of Chiral Fermions with a Large Topological Charge and Associated Fermi-Arc Surface States in CoSi, Phys. Rev. Lett. **122**, 076402 (2019).

[46] N. B. M. Schröter, D. Pei, M. G. Vergniory, Y. Sun, K. Manna, F. de Juan, J. A. Krieger, V. Süss, M. Schmidt, P. Dudin *et al.*, Chiral topological semimetal with multifold band crossings and long Fermi arcs, Nat. Phys.1 (2019).

[47] N. B. M. Schröter, S. Stolz, K. Manna, F. de Juan, M. G. Vergniory, J. A. Krieger, D. Pei, T. Schmitt, P. Dudin, T. K. Kim, C. Cacho, B. Bradlyn, H. Borrmann, M. Schmidt, R. Widmer, V. N. Strocov, and C. Felser, Observation and control of maximal chern numbers in a chiral topological semimetal, Science **369**, 179 (2020).

[48] M. Yao, K. Manna, Q. Yang, A. Fedorov, V. Voroshnin, B. V. Schwarze, J. Hornung, S. Chattopadhyay, Z. Sun, S. N. Guin, J. Wosnitza, H. Borrmann, C. Shekhar, N. Kumar, J. Fink, Y. Sun, and C. Felser, Observation of giant spin-split Fermi-arc with maximal Chern number in the chiral topological semimetal PtGa, Nat. Commun. **11**, 2033 (2020).

[49] P. Sessi, F.-R. Fan, F. Küster, K. Manna, N. B. M. Schröter, J.-R. Ji, S. Stolz, J. A. Krieger, D. Pei, T. K. Kim, P. Dudin, C.

Cacho, R. Widmer, H. Borrmann, W. Shi, K. Chang, Y. Sun, C. Felser, and S. S. P. Parkin, Handedness-dependent quasiparticle interference in the two enantiomers of the topological chiral semimetal PdGa, Nat. Commun. **11**, 3507 (2020).

[50] F. de Juan, A. G. Grushin, T. Morimoto, and J. E. Moore, Quantized circular photogalvanic effect in Weyl semimetals, Nat. Commun. **8**, 15995 (2017).

[51] E. J. König, H.-Y. Xie, D. A. Pesin, and A. Levchenko, Photogalvanic effect in Weyl semimetals, Phys. Rev. B **96**, 075123 (2017).

[52] F. Flicker, F. de Juan, B. Bradlyn, T. Morimoto, M. G. Vergniory, and A. G. Grushin, Chiral optical response of multifold fermions, Phys. Rev. B **98**, 155145 (2018).

[53] See Supplemental Material at http://link.aps.org/supplemental/10.1103/PhysRevResearch.4.L022022 for details on the experimental measurements, details on calculating the second-harmonic generation response function within the scissor approximation, the SHG in family of transition metal silicides, and further details on the low-energy model discussed in the main text.

[54] A. Gulans, S. Kontur, C. Meisenbichler, D. Nabok, P. Pavone, S. Rigamonti, S. Sagmeister, U. Werner, and C. Draxl, exciting: a full-potential all-electron package implementing density-functional theory and many-body perturbation theory, J. Phys.: Condens. Matter **26**, 363202 (2014).

[55] J. P. Perdew, K. Burke, and M. Ernzerhof, Generalized Gradient Approximation Made Simple, Phys. Rev. Lett. **77**, 3865 (1996).

[56] I. Engström and T. Johnsson, Least-squares refinement of the structure of RhSi (FeSi-type), Acta Chem. Scand. **19**, 1508 (1965).

[57] S. Bergfeld and W. Daum, Second-Harmonic Generation in GaAs: Experiment Versus Theoretical Predictions of $\chi^{(2)}_{xyz}$, Phys. Rev. Lett. **90**, 036801 (2003).

[58] L. Z. Tan and A. M. Rappe, Upper limit on shift current generation in extended systems, Phys. Rev. B **100**, 085102 (2019).